HiSST: 2nd International Conference on
High-Speed Vehicle Science & Technology
11–15 September 2022, Bruges, Belgium

Distributed Fuelling Schemes for Supersonic Combustion of Ethylene using Tandem Cavities in a Mach 8 Scramjet

Sarah Mecklem[1], *Damian Curran*[2], *Will Landsberg*[3], *Ananthanarayanan Veeraragavan*[4]

Abstract

A numerical comparison of distributed fuelling schemes was conducted using US3D Reynolds-Averaged Navier Stokes (RANS) for an ethylene-fuelled Mach 8 axisymmetric scramjet with tandem cavities. Three fuelling configurations were evaluated using a combination of injector ports located upstream, downstream, between, and within the tandem cavities - maintaining a consistent fuel-to-air equivalence ratio at 50% of stoichiometric. Combustion behaviour was compared between 'cold-wall' conditions, representing shock tunnel equivalent test conditions with minimal wall heating, and 'hot-wall' conditions, representing steady, in-fight wall temperatures. Under hot-wall conditions, a portion of the wall boundary represented a thermal sink for regenerative fuel heating. Mixing, fuel penetration, and total heat release were highest for the upstream-only (baseline) fuelling configuration, however the distributed fuelling schemes presented resulted in up to 29% less drag at the expense of a 9% reduction in total heat release. Distributed fuelling methods external to the cavity were more robust to changes in the thermal environment.

Keywords: *Tandem Cavity, Scramjet, Hypersonics, Combustion*

Nomenclature

Latin
A – Area
c – Specific heat
D – Cavity depth
$\dot{H}$ – Heat release, chemical
k – Thermal conductivity
L – Cavity length
$\dot{m}$ – Mass flux
N – Chemical species
Q – Heat
S – Strain rate
T – Temperature
u – Velocity
$\dot{w}$ – Reaction rate
Greek
η – Efficiency (/1)
$\mathbf{\Omega}$ – Vorticity
ϕ – Fuel-to-air equivalence ratio
ρ – Density
θ – Cavity closeout angle
∞ – Freestream
Superscripts
0 – Reference conditions
Subscripts
c – Combustion
f – Fuel
m – Mixing
p – Pressure
S – Stagnation
st – Stoichiometric
R – Reactant
t – Total (fuel)
w – Wall
0 – Primary (fuel)

[1]*Centre for Hypersonics, The University of Queensland, s.mecklem@uq.edu.au*
[2]*Centre for Hypersonics, The University of Queensland, d.curran@uq.edu.au*
[3]*Centre for Hypersonics, The University of Queensland, w.landsberg@uq.edu.au*
[4]*Centre for Hypersonics, The University of Queensland, anandv@uq.edu.au*

1. Introduction

Hydrocarbons are an ideal fuel for airframe-integrated scramjet engines owing to their increased energy density (MJ/m^3) over hydrogen; ca. eight (8) times for ethylene. These improvements come at the expense of a ten-fold increase to ignition delay time, being on the order of one (1) millisecond for ethylene at typical scramjet combustor conditions [1]. Given the air-residence time within a scramjet is also on the order of one (1) millisecond, this provides a challenging environment for mixing, ignition, and combustion processes to occur.

Wall-recessed cavity flame holders provide a passive mechanism of increasing air-residence time in addition to cultivating a sheltered region in which a flame may ignite and be sustained. A cavity flame holder is characterised by its depth (D), length-to-depth ratio (L/D), and a rear-wall closeout angle (θ), as shown in Figure 1. The cavity is ideally comprised of a large, primary vortex - typically oriented with the freestream - which is driven by freestream momentum transfer via the shear layer. The smaller, secondary vortex shown is driven through momentum exchange with the first, and rotates in opposition.

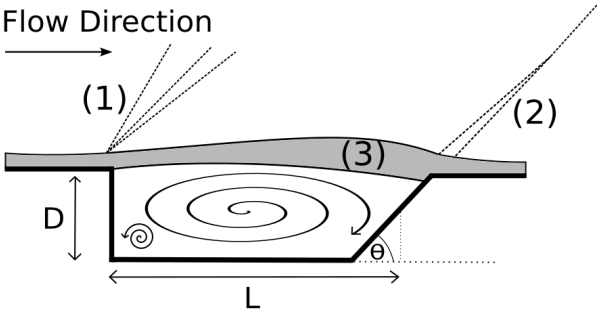

Fig 1. Canonical cavity description with (1) expansion fan generated at leading edge, (2) recompression shock at trailing edge, and (3) enclosing shear layer.

Numerous works have already demonstrated the importance of cavity flame holders for achieving ethylene ignition and flameholding within scramjets, e.g., [2]. Dual, or tandem, cavity arrangements have also been shown to increase stream thrust [3] and provide higher flame stability limits [4]. Recent work from [5] found mixing, combustion, and heat release achieved using tandem cavities were highly dependent on flameholding mode. Here, tandem cavities provided the most benefit when fuelling rates generated scram- or fully dual-mode combustion. Almost zero improvements occured when using a second cavity alongside jet-wake-anchored (JWA) combustion, in which the underexpanded fuel jet generated a momentum blockage significant enough to shelter and anchor a flame base within the fuel jet's wake. Despite providing a natural flameholding region, the resulting momentum blockages generated significant pressure losses and reduced scramjet thrust capability.

Equivalent quantities of fuel may instead be supplied through distributed fuelling methods, reducing the pressure losses sustained at the primary injection site, ideally without compromising on total heat release. Direct cavity fuelling has been investigated by [6, 7] with the greatest mixing improvments achieved by injecting fuel in a manner that reinforces the cavity's primary vortex. Combined fuelling (i.e., fuelling from within and external to the cavity) has been studied, with [8] finding the cavity environment to be susceptible to rich blow out (RBO) when supplied with up to 10% of the total fuel.

This work investigates the influence of distributed ethylene fuelling used in conjunction with tandem cavities. Additional fuelling sites are located within, between and downstream of the cavities. A total global fuel-to-air equivalence ratio of ϕ_t=0.5 is maintained for each fuelling configuration. Cold- and hot-wall boundaries are examined to compare between experimental facility and in-flight combustion behaviour.

2. Methodology

2.1. Flowpath Description

The axisymmetric Mach 8 scramjet combustor model utilised within this work is based on that developed in [9] which has been experimentally and numerically found to yield robust combustion at the ϕ_t=0.5 fuelling rate considered in this work [5, 10]. This model comprised a diffuser designed to deliver Mach 2.9 flow to the isolator, one or two cavity flameholders (L/D=4, D=8 mm θ=22.5°), a constant area combustor, then a diverging portion. For this previously examined model, fuel was supplied through one 2 mm diameter (⌀=2 mm) injector port located 22.5 mm upstream of the first cavity. A series of alterations were made to this model in the present study.

Several modifications were made to this model to ensure it operated at marginal flameholding limits. This included adopting a lower contraction-ratio inlet, designed to instead deliver Mach 3.1 flow to the isolator and reducing the baseline cavity depth from 8 mm (which ensured robust flameholding) to 4 mm. The primary injector port was resized to ⌀=1 mm to ensure adequate jet penetration is achieved at the lower upstream fuelling rates adopted for distributed fuelling. The second cavity was located to achieve an inter-cavity distance of 6D (i.e. 6 x 4 mm). Additional fuel ports were located within the first cavity, between and downstream of the two cavities. External fuel ports were sized as ⌀=1 mm and cavity-based fuel ports were $\oslash = \sqrt{2}/2$ mm. A flowpath schematic with injector locations is shown in Figure 2.

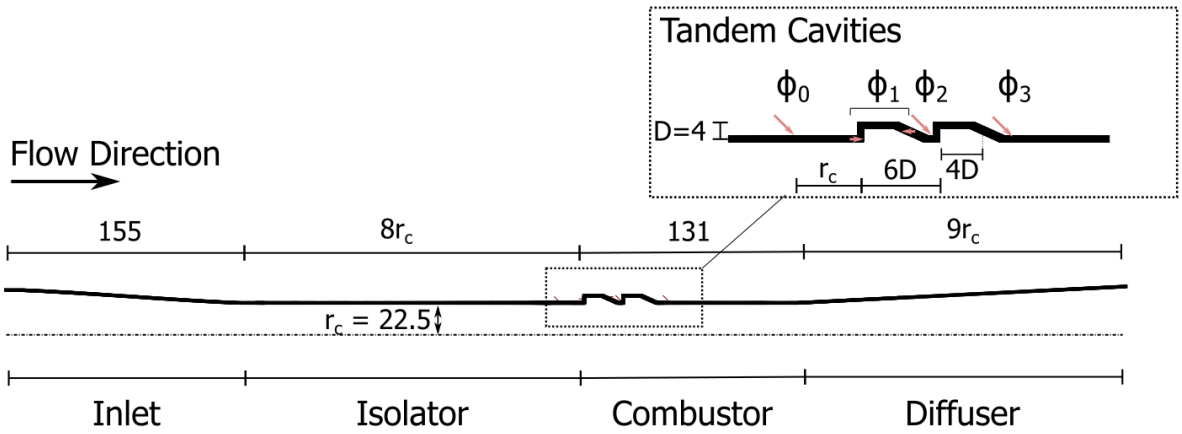

Fig 2. Axisymmetric scramet flowpath studied indicating locations of primary injector port (ϕ_0) and secondary injector ports (ϕ_1, ϕ_2, ϕ_3). All dimensions are in mm.

2.2. Computational Solver

Reacting three-dimensional solutions to the compressible Reynolds Averaged Navier Stokes (RANS) were solved using US3D [11]. US3D solves inviscid (convective) fluxes via the modified Steger-Warming flux splitting scheme and viscous fluxes via the central difference MUSCL scheme. Viscous and inviscid updates were determined implicitly with a second order accuracy. The turbulent Prandtl number and turbulent Schmidt number were set to 0.9 and 0.3, respectively. Turbulence quantities were evaluated using the Spalart Allmaras turbulence model [12] with the Catris-Aupiox compressibility correlation [13]. Thermally perfect gas, vibrational equilibrium and thermal equilibrium were assumed in this work. US3D solves Gibbs free energy parameters using NASA Lewis correlations [14] and flow chemisty using Arrhenius reaction coefficients. The ethylene reaction mechanism used within this work was a 6-species, 3-reaction skeletal mechanism detailed in [15].

Solutions for the cold-wall cases were generated assuming the flow remained laminar until the end of the inlet, at which point the reflected inlet compression shock trips the flow. Hence, flow from the isolator was fully turbulent. This solver configuration has been validated for the flow conditions and fuelling rates examined in this work using experimental facility data [5]. Inlet flow for the hot-wall case was modelled as turbulent to generate a smooth, axisymmetric heated boundary layer profile appropriate

for conducting these fundamental combustor studies. This modelling decision was deemed appropriate owing to the increased turbulent kinetic energy supplied at in-flight conditions.

2.3. Computational Meshes

Three-dimensional structured computational meshes were generated via Gridpro v6.8 [16]. A mesh convergence study following the methodology of [17] was previously conducted in [5] using three grids of increasing cell density incremented using the US3D configuration described prior. Grid total cell counts of 10.4M, 17.1M, and 29.6M were solved and determined temperature, pressure and H_2O mass fraction parameters were within 0.25% of their Richardson extrapolated values when using the 10.4M cell grid. This cell density was maintained within this work. This grid included viscous clustering at all wall boundaries with a first cell height of 0.7 μm, which corresponded with $y^+ \leq 1.5$. This work required a total cell count of 11.6M owing to the inclusion of the secondary cavity and additional fuel injection topologies.

Cold-wall and hot-wall boundary conditions were implemented within this work, to represent ground test facility and in-flight conditions, respectively. Cold-wall boundaries were maintained at an isothermal 300 K to represent the minimal wall heating experienced during shock tunnel tests. Hot-wall boundaries were either modelled as adiabatic or regeneratively cooled with ethylene being used as the heat sink. The benefits of regenerative cooling are two-fold: (1) combustor wall temperatures are lower meaning walls have less complex thermal requirements, and (2), fuel in cold storage is preheated prior to being injected which increases overall flammability. A simple heat exchanger model is proposed in this work in which ethylene (initally stored at 300 K) is heated to $T_{f,hot}$ prior to injection. Assuming perfect conversion, heat absorbed by the wall is equivalent to that absorbed by fuel to achieve this temperature change:

$$\begin{aligned} Q_f &= Q_w \\ \dot{m}_f c_p(T) \Delta T_f &= kA\Delta T_w dx \end{aligned} \tag{1}$$

Where Q_f and Q_w represent heat absorbed by fuel and supplied to the wall, respectively, $\dot{m}_f$ is the mass flow rate of fuel, c_p(T) is the average specific heat of the fuel over its temperature range ΔT_f - being ($T_{f,hot}$- 300 K). k is the thermal conductivity of fluid in the cell adjacent to the wall, hence also at the wall asuming equilibrium, A is the area of wall cooled, and ΔT_w is the temperature change at the wall effected by cooling - assumed as the difference between the adiabatic wall temperature and the cooled wall temperature. Wall temperature distributions were solved by varying A and $T_{f,hot}$ for the single injector case (ϕ_0 = 0.5) until a minumum temperature reduction of 1000 K was achieved. This resulted in $T_{f,hot}$ being 1000 K and A representing the constant area portion of the combustor. $T_{f,hot}$ and A remained constant for the hot-wall cases studied, with a unique temperature distribution supplied as the isothermal boundary condition for the cooled regions. Hence in the hot-wall configuration, all wall boundaries bar the combustor's constant area portion were modelled as adiabatic, with the entire length of the constant-area portion having a fixed temperature profile representative of the steady-state regenerative cooling effect.

Inflow and fuelling conditions studied for the cold-wall and hot-wall domains are presented in Tables 1 and 2, respectively. Where injected, fuel was supplied at sonic conditions and was assumed to undergo isentropic expansion. Cold fuel was supplied with a stagnation temperature of 300 K.

Table 1. Inflow conditions

Parameter	Value	Unit
Freestream Conditions		
Stagnation enthalpy (H_s)	2.65	$MJ.kg^{-1}$
Flight Mach number	7.4	-
Domain Inflow Conditions		
Mach number (M_∞)	3.81	-
Pressure (p_∞)	32.80	kPa
Temperature (T_∞)	832.0	K
Streamwise velocity (u_∞)	2203	$m.s^{-1}$
Density (ρ_∞)	0.137	$kg.m^{-3}$

Table 2. Fuelling configurations (ϕ_t=0.5)

Configuration	ϕ_0	ϕ_1 [1]	ϕ_2	ϕ_3
A	0.50	0.0	0.0	0.0
B	0.25	0.025	0.10	0.10
C	0.25	0.0	0.15	0.10

3. Results

Scramjet performance will be assessed using the following parameters: mixing efficiency, heat release, and total drag with consideration of physical characteristics such as jet penetration and vorticity to aid in explaining various combustion based phenomena. First, the overall flow fields are presented.

3.1. Flow Behaviour

Mach number contours resulting from each fuelling configuration and wall temperature distribution are shown in Figure 3, represented as the coaxial surfaces aligning with primary (top) and secondary (bottom) injectors. The corresponding mass flow weighted-averaged pressure and temperature distributions are also shown with respect to the combustor's geometry.

[1] Supplied at each of the two internal cavity injectors.

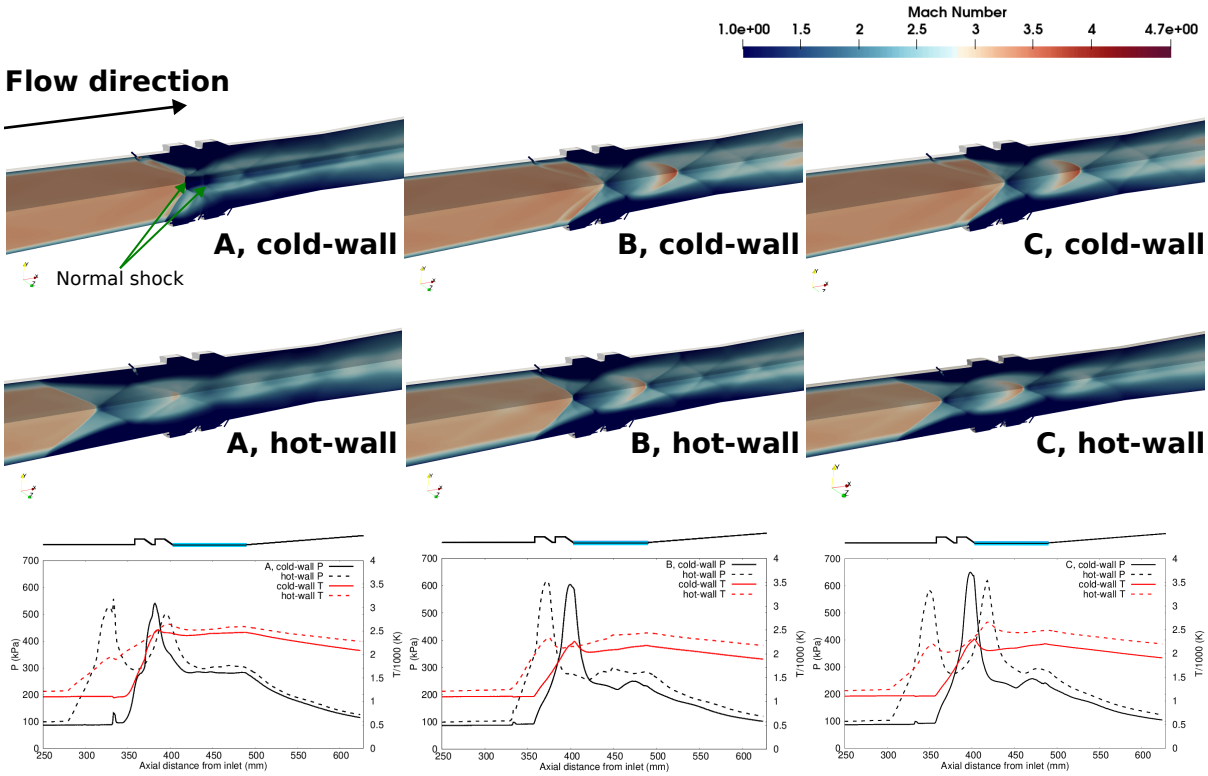

Fig 3. Rows 1 and 2: Mach number visualisation for each injector's coplanar axis under cold-wall and hot-wall conditions. Row 3: mass flow rate-averaged pressure (black) and temperature (red) distributions within the combustor. The regeneratively cooled portion of wall modelled under 'hot-wall' conditions is shown in blue.

Configuration **A** resulted in JWA combustion while configurations **B** and **C** both resulted in cavity-anchored combustion under cold-wall conditions. Cold-wall pressure distributions for the cavity-anchored cases show the pressure peak at the downstream cavity's trailing edge - coinciding with the highest temperature region within the flowpath - indicating robust combustion and heat release. The equivalent pressure peak seen in configuration **A** is approximately aligned with the mid-way point between the two cavities. This high pressure is the result of the normal shock structure train that begins to form in the core flow - indicated on Figure 3 - initiated through the formation of a separated region downstream of injector ϕ_0.

Simulated hot-wall conditions resulted in earlier flow separation for all fuelling configurations. Under these conditions, configurations **A** and **C** transitioned to full dual-mode operation in which the majority of flow within the combustor's core no longer remained supersonic and shock dominated. Configuration **B** transitioned from scram- to JWA combustion with flow separation commencing just prior to injector ϕ_0. This earlier flow separation was initiated under the hot-wall conditions owing to the increased adverse pressure gradients introduced through the combustion-induced pressure rise [18]. The earliest onset of boundary layer separation is seen at approximately 280 mm from the inlet for case **A** in the hot-wall condition where the thicker boundary layers in conjunction with less wall-based heat losses attributed to higher core flow temperatures and pressures than the cold-wall case. These conditions reduced ethylene's ignition delay time, hence facilitating earlier and more rapid combustion [19]. Fuelling configuration **B** resisted fully transitioning to dual-mode, hence facilitates stable operation under both cold- and hot-wall conditions.

Next, fuel penetration and the subsequent impact on mixing is discussed. Fuel penetration is characterised using the stoichiometric fuel-air boundary, shown as the solid white line in Figure 4. The mixing efficiency shown at each slice represents the proportion of fuel mass flux available in each cell available to react - if under infinitely fast chemistry - to the total fuel mass flux. This relationship is shown in Equation 2, where α is the fuel mass fraction, and α_R is the mass fraction of least available reactant when compared to stoichiometric proportions, α_{st}.

$$\eta_m = \frac{\int \alpha_R \rho u dA}{\int \alpha \rho u dA}, \quad \text{where } \alpha_R = \left\{ \begin{array}{ll} \alpha, & \text{for } \alpha \leq \alpha_{st} \\ \alpha_{st}\left(\frac{1-\alpha}{\alpha-\alpha_{st}}\right), & \text{for } \alpha > \alpha_{st} \end{array} \right\} \tag{2}$$

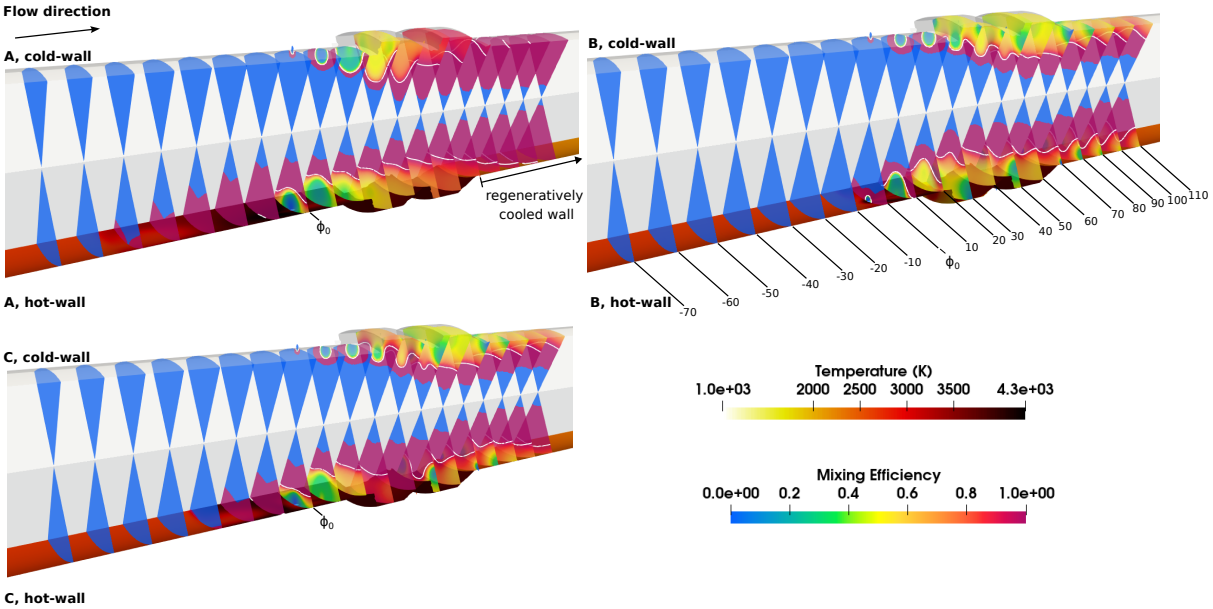

Fig 4. Sliced combustor sections showing mixing efficiency contours and stoichiometric fuel-air boundary in white. Slices for configuration **B** are shown with relative distance in mm from primary injector ϕ_0. This spacing is consistent for each depiction with numerical increments not replicated for clarity. Temperature contours for the hot-wall case are also shown.

Near-field penetration at ϕ_0 is higher in the hot-wall cases for all configurations owing to the hot fuel's increased diffusivity; hence a greater fraction of the slice appears fully mixed (for example, configuration **B** slices at 10 mm and 20 mm from ϕ_0). Slices upstream of injector ϕ_0 for dual-mode configurations **A** and **C** (at -10 mm and -20 mm) show either no or complete mixing. These slices are without a visible stoichiometric contour, indicating the region is fuel-lean (i.e., ϕ <1). High wall temperatures at these regions also demonstrate this separated region to be a location for flameholding.

Vorticial flow field structures for configurations **A** and **B** under cold-wall conditions are highlighted in Figure 5 which examines each solution's Q-criterion ($Q = \frac{1}{2}\left(||\mathbf{\Omega}||^2 - ||S||^2\right)$) [20]. This non-dimensional parameter represents the relative strength of the vorticity tensor's ($\mathbf{\Omega}$) magnitude to the strain rate tensor's (S) magnitude, hence indicating regions where rotational components of the flow dominate over strain-dominated or "stretched" regions. Configuration **A**'s cold-wall case shows the development of the counter-rotating vortex pair (CRVP) directly downstream of injector ϕ_0, in addition to horseshoe vortices (HV_1, HV_2), annotated on Figure 5. Next, a series of shear layer vortex structures (SLV_1, SLV_2) are generated as a result of curvature in the shear layer - indicated through the semi-transparent shroud in addition to black sonic contours mapped on each slice. The next series of vortex structures are generated within the leading cavity (CV). Flow previously redirected around the ϕ_0 fuel jet is drawn into the cavity and entrained into the primary vortex structure, which peaks in strength at the cavity's

sloped trailing edge as the recirculation region is redirected laterally back into the cavity. Downstream of the first cavity an additional series of shear layer vorticies are generated (SLV_3, SLV_4). The secondary cavity displays a comparably weaker vortex structure with no further structures meeting the minimum Q=1E10 threshold utilised within the iso-contours of Figure 5.

Configuration **B** reveals fewer vortex structures of equivalent strength to that seen in **A**. Injector-based vortex structures (HV, CRVP at ϕ_0) are less prevalent owing to the smaller fuel mass flux injected at ϕ_0. The shear layer vortex structures seen from the first cavity's leading edge coincide with the 'w' shaped sonic boundary, but these fail to span the length of the first cavity. No vortices of equivalent strength to that seen in configuration **A** emerged from the leading cavity, with the next major SLV structure being downstream of the second cavity. Distributed fuel injection from $\phi_1, \phi_2,$ and ϕ_3 did not impart signifant vorticity to the flow as this injection was directly into a subsonic region. The vortex structure for configuration **C** at cold-wall conditions is similar to that of **B** and is therefore not replicated here.

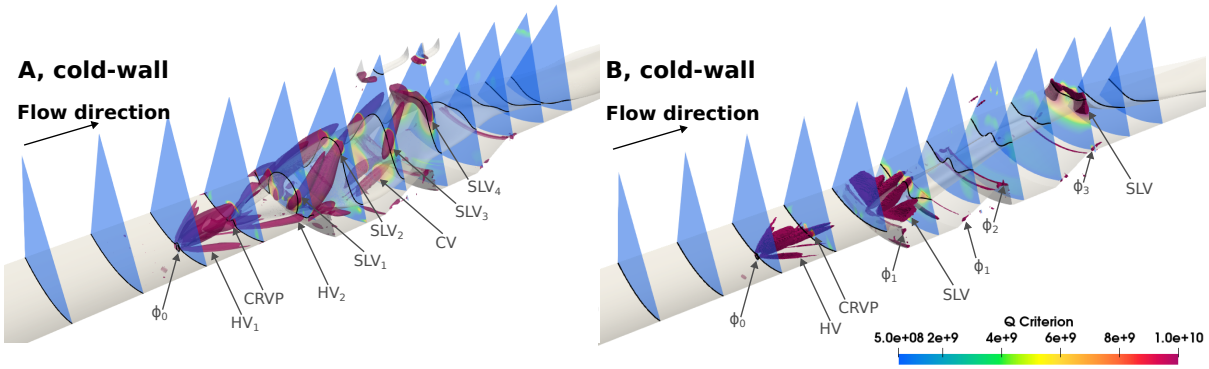

Fig 5. Sliced combustor sections showing thresholded Q-Criterion (Q) regions 1E8$\leq$ Q $\leq$ 1E10 for fuelling configurations **A** (left) and **B** (right) under cold-wall conditions. Iso-contours for Q=1E10 highlight dominant vortex structures. Shear layer development is indicated with a transparent sonic "shroud" which maps the intercepting sonic boundary as black lines on each slice. Refer to body for annotation definitions.

Vortex structures resulting from hot-wall conditions for fuelling configurations **A** and **B** are presented in Figure 6. Q-criterion iso-contours show the CRVP and HV eminated from injector ϕ_0 at both fuelling configurations are broader owing to the smaller strain rate experienced from injection into the surrounding subsonic flow. These, and the SLV seen at the shear layer's apex are the only dominant vortex structures at the Q=1E10 threshold previously examined for the cold-wall domains. Small vortex structures are seen at ϕ_1, ϕ_2 and ϕ_3 injector sites for fuelling configuration **B**, however these quickly dissipate.

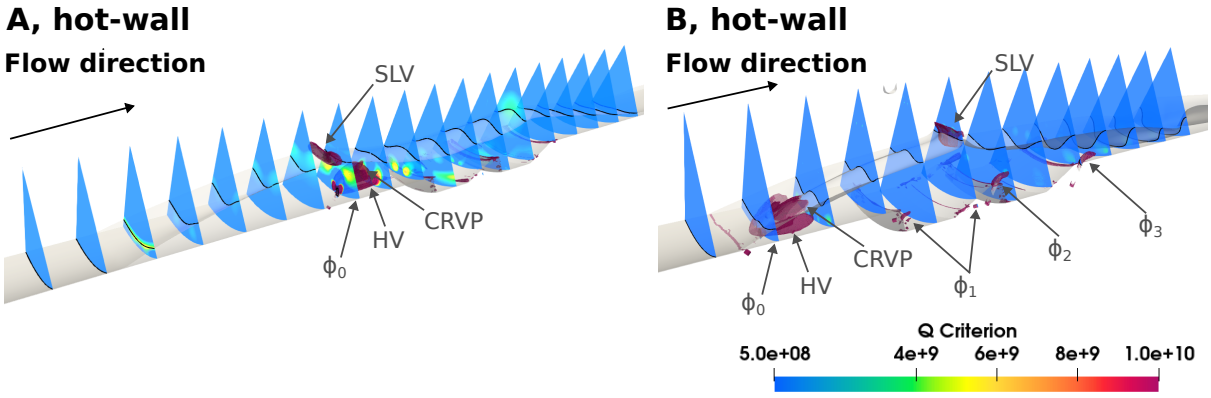

Fig 6. Sliced combustor sections showing thresholded Q-Criterion (Q) regions 1E8$\leq$ Q $\leq$ 1E10 for fuelling configurations **A** (left) and **B** (right) under hot-wall conditions.

Examples of hot-wall flow streamlines resulting from configuration **A** and **C**'s dual-mode operation and **B**'s JWA mode are highlighted in Figure 7. The upstream separation region in configuration **A** attributed with dual-mode operation houses a large recirculation region (S_{A1}); this facilitates the complete mixing previously seen upstream of injector ϕ_0 in Figure 4. From here, a portion of flow is redirected around the primary injector and enters the first cavity (S_{A2}) forming the recirculation region seen oriented with the direction of core flow, on the XY plane. The second cavity operates in a similar manner, with its primary recirculation region (S_{A3}) oriented in the same fashion. Streamlines for configuration **B** reveal a portion of flow entering the first cavity is first recirculated in the sheltered region behind the jet-wake (S_{B1}). Again, the first cavity's primary recirculation region is oriented with the XY plane. No significant flow disruptions resulted from directly injecting fuel into the cavity; recall this was done in a manner to reinforce this primary vortex. The second cavity's primary vortex (S_{B2}) is tilted around the X-axis as incoming flow must first be redirected around injector ϕ_2. S_{B2} also appears compressed, reducing the cavity's effective recirculation volume. This is attributed to upstream influence of high pressure flow expanding from injector ϕ_3 injector in conjuction with the low pressure seen in the second cavity (relative to the first). Vortex and streamline structures for configuration **C** appear as a combination of configuration **A** and **B** with S_{C1} being a combination of S_{A1} and the JWA portion of S_{B1}. Remaining S_{C2} and S_{C3} streamlines are similar to that seen in configuration **B**.

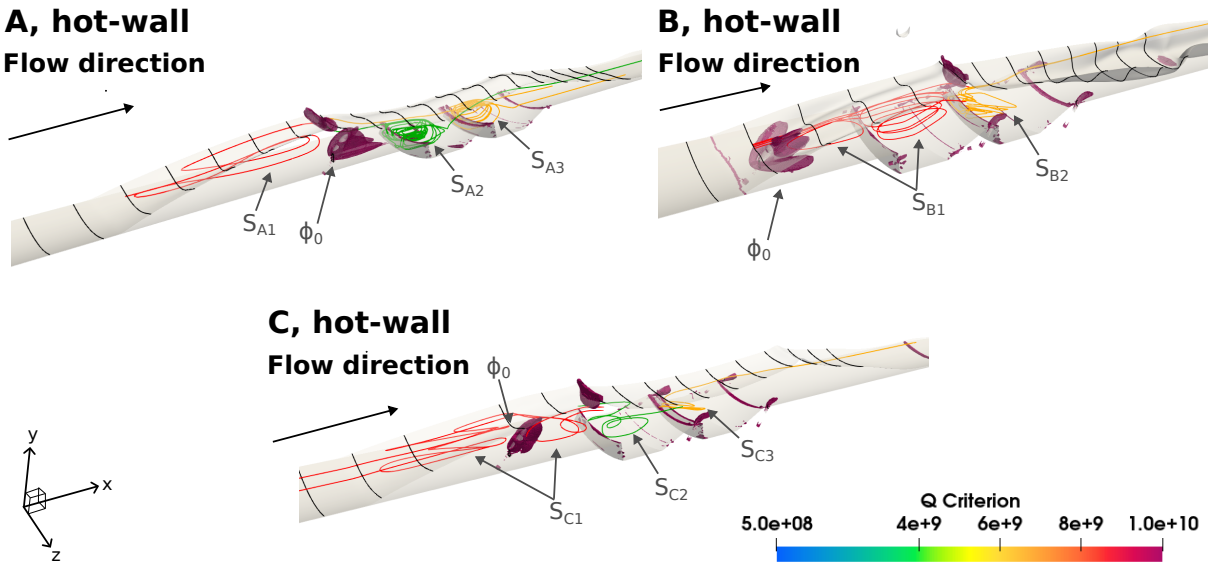

Fig 7. Streamline traces highight significant recirculation regions in relation to vortex structures indicated through regions where Q≥1E10. Annotated streamlines are coloured individually and have not been reflected on the symmetry plane for clarity. Refer to body for annotation definitions.

3.2. Combustor Performance

Combustor performance is now explored in terms of cumulative heat release and accrued drag, where drag is the summation of axial viscous and pressure drag components extracted from the domain's wall boundary. Note, the flowpath examined in this work does not contain a thrust-optimised inlet or diffuser; consequently, drag values presented should be considered in a relative context only.

Cumulative heat release is determined through the summation of instantaneous heat release [$\dot{H}$ (kW/m)] at each axial location within the combustor; with instantaneous heat release, per Equation 3, being the summed product of each flow species' (N) Arrhenius reaction rate ($\dot{w}_i$) by their respective heat of formation ($h^0_{f,i}$).

$$\dot{H} = \sum_{i}^{N} \left(\dot{w}_i \times {h_{f,i}}^0(T) \right) \tag{3}$$

Cumulative heat and drag for cold-wall and hot-wall flow conditions are summarised in Tables 3 and 4, respectively, which includes the relative difference of each parameter with respect to the baseline single-port fuelling configuration **A**. Distributed fuelling under cold- and hot-wall conditions lead to a moderate reduction in total heat release, with configuration **C** yielding a 2-3% improvement over **B**.

Both distributed fuelling schemes generated up to 29% less drag in the cold-wall configuration when compared to single-port fuelling as a result of both distributed methods functioning under scram-mode operation instead of sustaining increased pressure losses under the JWA mode. The desired scram-type operation was not replicated under the hot-wall conditions, hence equivalent drag reductions with distributed fuelling were not observed. A 3% reduction in drag was accomplished under fuelling configuration **C**, indicating this method of supplying supplemental fuel external to cavities is robust under both cold- and hot-wall conditions.

Table 3. End of domain cumulative heat release (kW) and total drag (N) for cold-wall conditions. Relative differences as compared with configuration **A** are shown in paretheses.

Configuration	$\Sigma\dot{H}$ (kW)		Drag (N)	
A	78.2		5.2	
B	69.6	(-11%)	3.8	(-27%)
C	70.1	(-9%)	3.7	(-29%)

Table 4. End of domain cumulative heat release (kW) and total drag (N) for hot-wall conditions. Relative differences as compared with configuration **A** are shown in paretheses.

Configuration	$\Sigma\dot{H}$ (kW)		Drag (N)	
A	76.8		3.5	
B	70.2	(-9%)	3.7	(+5%)
C	72.0	(-6%)	3.4	(-3%)

4. Conclusion

Distributed ethylene fuelling schemes were examined for a tandem-cavity equipped scramjet combustor under ground-test facility conditions (termed 'cold-wall') and simulated flight conditions ('hot-wall') in comparison with a baseline single-port injection scheme **A**. A total fuel-to-air equivalence ratio of 50% stoichiometric was maintained between each fuelling configuration. Distributed fuelling schemes **B** and **C** were both supplied with half the mass flux of **A** at the primary injector ϕ_0, with the remaining half reallocated to fuel ports within the leading cavity, between the two cavities, and just downstream of the second cavity.

Inspection of flowfield structures, such as vorticity via the Q-criterion, revealed the majority of mixing acceleration was achieved via jet-affiliated vortex structures and shear-layer vorticies spanning over the cavity region. Equivalent levels of vorticity were not generated from injecting fuel directly into the cavity per configuration **B**, which resulted in inhibited mixing within the injected cavity.

Single-port injection resulted in higher fuel penetration under both cold- and hot-wall conditions, yielding improved core-flow mixing and total heat release - up to 11% in the cold-wall case. This discrete fuelling strategy garnered higher losses, with 29% more drag than distributed fuelling strategy **C** under cold-wall conditions, and 3% more in hot-wall conditions. Fuelling strategy **B** resisted transitioning to full dual-mode operation under hot-wall conditions, and remained in scram-mode at cold-wall conditions; this modal stability is ideal for pursuing reliable and repeatable scramjet combustion behaviour. The marginal heat losses sustained under distributed fuelling configurations **B** and **C** show merit in employing distributed fuelling strategies in conjunction with tandem cavity flameholders.

5. Acknowledgements

This research was a collaboration between the Commonwealth of Australia (represented by the Defence Science and Technology Group) and the University of Queensland, through a Defence Science Partnerships agreement. A. Veeraragavan acknowledges the support from his Advance Queensland Research Fellowship. This work was supported by resources provided by the Pawsey Supercomputing Research Centre with funding from the Australian Government and the Government of Western Australia.

References

[1] Z. J. Denman, V. Wheatley, M. K. Smart, A. Veeraragavan, Supersonic combustion of hydrocarbons in a shape-transitioning hypersonic engine, Proceedings of the Combustion Institute 36 (2) (2017) 2883–2891.

[2] W. O. Landsberg, T. Vanyai, T. J. McIntyre, A. Veeraragavan, Experimental scramjet combustion modes of hydrocarbon mixtures at mach 8 flight conditions, AIAA Journal 58 (12) (2020) 5117–5122.

[3] M. Collatz, M. Gruber, D. Olmstead, R. Branam, K.-C. Lin, C.-J. Tam, Dual cavity scramjet operability and performance study, in: 45th AIAA/ASME/SAE/ASEE Joint Propulsion Conference & Exhibit, 2009, p. 5030.

[4] Y. Pan, J.-G. Tan, J.-H. Liang, W.-D. Liu, Z.-G. Wang, Experimental investigation of combustion mechanisms of kerosene-fueled scramjet engines with double-cavity flameholders, Acta Mechanica Sinica 27 (6) (2011) 891–897.

[5] S. A. Mecklem, W. O. Landsberg, D. Curran, A. Veeraragavan, Combustion enhancement via tandem cavities within a mach 8 scramjet combustor, Aerospace Science and Technology 124 (2022) 107551.

[6] M. R. Gruber, J. M. Donbar, C. D. Carter, K.-Y. Hsu, Mixing and combustion studies using cavity-based flameholders in a supersonic flow, Journal of Propulsion and Power 20 (5) (2004) 769–778.

[7] H. B. Ebrahimi, F. J. Malo-Molina, D. V. Gaitonde, Numerical simulation of injection strategies in a cavity-based supersonic combustor, Journal of Propulsion and Power 28 (5) (2012) 991–999.

[8] K.-C. Lin, C.-J. Tam, I. Boxx, C. Carter, K. Jackson, M. Lindsey, Flame characteristics and fuel entrainment inside a cavity flame holder in a scramjet combustor (postprint), Tech. rep., TAITECH INC BEAVERCREEK OH (2007).

[9] T. Vanyai, S. Grieve, O. Street, Z. Denman, T. McIntyre, A. Veeraragavan, V. Wheatley, M. Smart, Fundamental scramjet combustion experiments using hydrocarbon fuel, Journal of Propulsion and Power 35 (5) (2019) 953–963.

[10] W. O. Landsberg, D. Curran, A. Veeraragavan, Influence of cavity depth on ignition and flameholding modes within a scramjet combustor, in: ASCEND 2021, 2021, p. 4163.

[11] I. Nompelis, T. Drayna, G. Candler, Development of a hybrid unstructured implicit solver for the simulation of reacting flows over complex geometries, in: 34th AIAA Fluid Dynamics Conference and Exhibit, 2004, p. 2227.

[12] P. Spalart, S. Allmaras, A one-equation turbulence model for aerodynamic flows, in: 30th aerospace sciences meeting and exhibit, 1992, p. 439.

[13] S. Catris, B. Aupoix, Density corrections for turbulence models, Aerospace Science and Technology 4 (1) (2000) 1–11.

[14] S. Gordon, B. J. McBride, Computer program for calculation of complex chemical equilibrium, NASA reference publication, 1994 (1994).

[15] R. Baurle, D. Eklund, Analysis of dual-mode hydrocarbon scramjet operation at mach 4-6.5, Journal of Propulsion and Power 18 (5) (2002) 990–1002.

[16] GridPro, GridPro GUI Manual, Program Development Company, White Plains, NY 10601, gUI Version 6.6 (2017).

[17] F. Stern, R. V. Wilson, H. W. Coleman, E. G. Paterson, Comprehensive approach to verification and validation of cfd simulations—part 1: methodology and procedures, J. Fluids Eng. 123 (4) (2001) 793–802.

[18] M. A. Frost, D. Y. Gangurde, A. Paull, D. J. Mee, Boundary-layer separation due to combustion-induced pressure rise in a supersonic flow, AIAA journal 47 (4) (2009) 1050–1053.

[19] M. I. Colket, L. Spadaccini, Scramjet fuels autoignition study, Journal of Propulsion and Power 17 (2) (2001) 315–323. doi:10.2514/2.5744.

[20] J. Jeong, F. Hussain, On the identification of a vortex, Journal of fluid mechanics 285 (1995) 69–94.